Cronfa - Swansea University Open Access Repository

_____

_____

_____

_____

The role of bulk and interface recombination in high efficiency low dimensional perovskite solar cells

Shanshan Zhang[1,2], Seyed M. Hosseini[1], René Gunder[3], Andrei Petsiuk[3], Pietro Caprioglio[1], Christian M. Wolff[1], Safa Shoaee[1], Paul Meredith[4], Susan Schorr[3], Thomas Unold[3], Paul L. Burn[2], Dieter Neher[1], Martin Stolterfoht[1,*]

[1]Institute of Physics and Astronomy, University of Potsdam, Karl-Liebknecht-Str. 24-25, D-14476 Potsdam-Golm, Germany

[2]Centre for Organic Photonics & Electronics (COPE), School of Chemistry and Molecular Biosciences, The University of Queensland, Brisbane 4072, Australia

[3]Department of Structure and Dynamics of Energy Materials, Helmholtz-Zentrum-Berlin, Hahn-Meitner-Platz 1, D-14109 Berlin, Germany

[4]Department of Physics, Swansea University, Singleton Park, Swansea SA2 8PP Wales, United Kingdom

E-mail: stolterf@uni-potsdam.de

Abstract

Two-dimensional Ruddlesden–Popper perovskite (RPP) solar cells have received significant attention due to their excellent environmental stability. However, the power conversion efficiency (PCE) of RPP cells is still inferior to 3D perovskites. Herein, we analysed two-dimensional $(CH_3(CH_2)_3NH_3)_2(CH_3NH_3)_{n-1}Pb_nI_{3n+1}$ perovskite cells with different numbers of $[PbI_6]^{4-}$ sheets (n = 2—4). Photoluminescence quantum yield (PLQY) measurements showed that non-radiative open-circuit voltage (V_{OC}) losses outweighed radiative V_{OC} losses in materials with $n > 2$, while the opposite was the case for the n = 2 system due to its excitonic nature. The n = 3 and n = 4 films exhibited a higher PLQY than the standard 3D MAPI perovskite although this was accompanied by increased interfacial recombination at the top perovskite/C_{60} interface. Overall, this trade-off resulted in a similar PLQY in all devices, including the n = 2 system where the perovskite bulk dominates the recombination properties of the cell. The quasi-Fermi level splitting (QFLS) of most cells was found to match the device V_{OC} within 20 meV, which indicated minimal recombination losses at the metal contacts. We also found that poor charge transport, especially in the n = 2 compound, rather than field-dependent exciton dissociation is the primary reason for the substantial reduction in fill factor of the RPP devices. Optimized RPP solar cells with n = 4 exhibited PCEs of nearly 15% with significant potential for further improvements through suppression of interfacial recombination and better charge transport.

Introduction

Organic-inorganic halide perovskite solar cells are an emerging photovoltaic technology that has seen power conversion efficiencies (PCEs) surging from 3.9% to 23.7%[1] within approximately 10 years. Considering their superior opto-electronic properties, it is predicted that perovskite solar cells could reach efficiencies comparable to monocrystalline silicon solar cells.[2] Given these excellent efficiencies and the ongoing technological potential, attention is now increasingly focused on the stability of the constituent materials. The development of both high-efficiency and stable devices and/or environmentally benign perovskites is a critical yet challenging task due to the ionic nature of the most promising photovoltaic perovskites. Compared to traditional inorganic semiconductors, current hybrid organic-inorganic perovskite materials that are useful in solar cells decompose comparatively quickly under environmental stresses such as exposure to moisture, oxygen and heat, and continuous illumination.[3] Layered two-dimensional Ruddlesden-Popper perovskites (RPPs) which are a multiple quantum well structures, where a defined number of $[PbI_6]^{4-}$ layers sheets is interleaved with double layers of organic cations are more tolerant to moisture than common three-dimensional perovskites, which has been ascribed to the water repellent nature of the aliphatic carbon chains in the perovskite lattice.[4],[5] Benefiting from this feature, a layered perovskite (film) with enhanced moisture stability of up to 40 days was reported by Smith et al in 2014.[6] As with many new concepts the initial power conversion efficiencies (PCEs) of solar cells containing the two-dimensional perovskites were relatively low. However, the photovoltaic performance of such materials has improved with a PCE of 12.5% reported by Tsai *et al.* in 2016.[7] In that report, the $[PbI_6]^{4-}$ layer sheets were oriented normal to the substrate, which facilitated the charge transport. Notably, an un-encapsulated layered perovskite $(BA)_2(MA)_3Pb_4I_{13}$ device was reported to retain >60% of its efficiency over 2,250 hours and also displayed a greater tolerance to 65% relative humidity compared to a three-dimensional perovskite. Recently, through compositional engineering, PCEs approaching 14% have been achieved with a Cs doped $(BA)_2(MA)_3Pb_4I_{13}$ active layer[8]. Furthermore, a new type of layered perovskite with a nanorod-like morphology was reported with an efficiency exceeding 15%[9]. An elegant approach to balance stability and efficiency has been to deposit a thin layer of two-dimensional perovskite as a cap on the top of a three-dimensional perovskite structure or mixing two- and three-dimensional perovskite precursors to form a so called 2D/3D perovskite.[10],[11],[12] Using such a strategy, Grancini et al. showed a device with a PCE of 11.2% that was stable for >10,000 h under continuous illumination and short-circuit conditions at 55 °C.[13]

The optoelectronic properties of the two-dimensional perovskites can be tuned by modifying the chemical composition of organic spacers, which influences the confinement of charges in the $[PbI_6]^{4-}$ sheets. In this regard, studies on two-dimensional RPP quantum-well-like materials have reported photoluminescence quantum yields (PLQY) close to 35%, which was achieved by reducing the layer thickness and changing the two-dimensional perovskite constituent ions.[14] ,[15],[16],[17] As a consequence, RRP materials are also of interest for light emitting diode applications.[18],[19],[20],[21] In order to reveal the charge carrier dynamics and energy transfer through the quantum-wells, several studies have combined transient absorption (TAS) and transient photoluminescence (TRPL) measurements to study the effect of the different organic spacers and numbers of $[PbI_6]^{4-}$ layers (*n*).[22],[23],[24],[25] Charge carrier recombination and out-of-plane mobilities in two-dimensional perovskite films have also been investigated by time-resolved terahertz (THz) spectroscopy.[26] It was observed that when an increasing amount of two-dimensional phenylethylammonium (PEA) lead iodide was mixed with the three-dimensional methylammonium lead iodide (MAPI), traps were effectively passivated in the perovskite bulk. However, the mixing caused an

increase in the first-order recombination rates due to enhanced excitonic effects in the thin confined layers. Moreover, a comparatively high carrier mobility close to $10\ cm^2V^{-1}s^{-1}$ was found for the intermediate 50% PEA content film corresponding to a charge-carrier diffusion length of 2.5 µm (parallel to the sheets). Excitonic many-body interactions in two-dimensional $BA_2MA_{n-1}Pb_nI3_{n+1}$ (n = 1−3) based perovskites were also studied by Wu et al.[27] who observed an excitonic blue-shift and localization using transient-absorption spectroscopy (TAS) at room temperature. Despite this progress, many important fundamental aspects of charge transport and recombination loss mechanism remain to be determined. Among, the most important questions in this regard is the nature and the origin of the non-radiative recombination losses which limit the open-circuit voltage (V_{OC}) and the fill factor of the cells.[28,29] In particular, the relative importance of interfacial or contact recombination versus radiative and non-radiative recombination in the perovskite bulk remains an unknown but essential question. Moreover, the exact mechanism behind the generally low fill factors (FFs) in two-dimensional perovskite cells is not well understood. While several studies point to inefficient charge extraction in causing the FF losses,[30],[31] the role of field-dependent charge generation on the FF in these quantum confined systems has not been elucidated. A comprehensive understanding of all these loss processes is important to enable advancement in the efficiency of two-dimensional perovskite solar cells.

In this work we present a quantitative electro-optical study that reveals the energy and charge transport loss mechanisms in two-dimensional perovskites based on n-butylammonium iodide (BA) (n = 2−4). In the first part of the study, we analyzed the morphology of the perovskites films using X-ray diffraction. The measurements revealed a preferred $[PbI_6]^{4-}$ layer orientation normal to the substrate for the $BA_2MA_2Pb_3I_{10}$ ("BA3"), and $BA_2MA_3Pb_4I_{13}$ ("BA4") perovskites, while the $[PbI_6]^{4-}$ sheets were parallel to the substrate in the case of $BA_2MAPb_2I_7$ ("BA2"). We then used transient and absolute PL in combination with electroluminescence measurements to disentangle the relative contributions of radiative and non-radiative recombination losses in the perovskite bulk, at the interfaces with the organic charge transport layers and at the metal contacts. Trap-assisted recombination in the absorber layer was found to be less severe for the BA3 and BA4 films compared to MAPI. Moreover, introduction of the hole-transport layer (HTL) PTAA/PFN-Br [Poly(bis{4-phenyl}{2,4,6-trimethylphenyl}amine)]/[poly({9,9-bis[30-({N,N-dimethyl}-N-ethylammonium)-propyl]-2,7-fluorene}-alt-2,7-{9,9-di-n-octylfluorene})dibromide] effectively passivated the perovskite bottom surface potentially allowing open-circuit voltages of 1.23 V for the BA3- and BA4-based cells. However, the V_{OC} of the complete cells was strongly limited by recombination at the perovskite/C_{60} interface, which resulted in a device V_{OC} below 1.2 V. In addition, we used intensity dependent photocurrent (IPC),[32,33] integral time of flight (iTOF)[29] and time delayed collection field (TDCF)[34] experiments to understand the reason for the significant FF losses in the two-dimensional perovskite samples. IPC revealed that the charge carrier collection of BA3, BA4 and MAPI solar cells was not affected by second-order bimolecular recombination of free charges under 1-sun and short-circuit conditions. However, substantial bimolecular losses were observed for the BA2-based cells which was consistent with a substantial slowing of charge extraction as observed using iTOF for the BA2 active layer. Moreover, TDCF measurements demonstrated field-independent charge generation for all the perovskite materials, meaning that the FF was not limited by (geminate) recombination of photogenerated excitons. This led to the conclusion that insufficient extraction of free charges was the primary reason for the low FF in the two-dimensional perovskite solar cells. Thus, the work elucidates the reasons behind the lower performance of the two-dimensional perovskite devices and highlights new strategies towards creating highly efficient and stable perovskite solar cells.

Results:

Device performance and optical properties of MAPI and two-dimensional layered perovskites.

In the first part of the study we investigated the layered perovskite family $BA_2MA_{n-1}Pb_nI_{3n+1}$ (n = 2-4) as well as the three-dimensional perovskite, methylammonium lead iodide (MAPI), in a planar p–i–n device configuration. Adding n-butylammonium iodide as the organic spacer in RPPs transforms the 3D network of the corner-shared octahedra of organohalide perovskites of the general form $CH_3NH_3PbX_3$ (X = I, Br, Cl) into a two-dimensional network of perovskite layers with intercalated organic bilayers. The sum formula is given as $[(CH_3(CH_2)_3NH_3)_2(CH_3NH_3)_{n-1}Pb_nX_{3+n}]$, where the integer n reflects the ratio between the n-butylammonium halide, methyl ammonium halide and lead halide that, in turn, determines the layer periodicity between interconnected sheets of the $[PbI_6]^{4-}$ octahedra and $[CH_3(CH_2)_3NH_3]^+$ bilayers. The commonly used p-type interlayer poly(3,4-ethylenedioxythiophene):polystyrene sulfonate (PEDOT:PSS) was replaced by PTAA/PFN-Br and 5wt% CsI was included in perovskite solution for improving the film quality.[8] An excellent PCE of 14.9% was achieved with a BA4 device (see **Table 1**) via a hot casting process.[7] Notably, compared to the literature,[7],[35] the BA3 and BA2 cells showed relatively good efficiencies of 11% and 1.4%, respectively, with a continuous drop in performance with decreasing number of layers n . **Figure 1 (a)** shows the JVs of the best devices, with the average performance parameters for 12 devices summarized in **Table 1**. The performance of the individual cells is plotted in **Supplementary Figure S1**. In particular, we found that the FF and the short-circuit current density (J_{SC}) drop continuously going from the three-dimensional (MAPI) to the two-dimensional perovskites and decreasing n, while the BA4- and BA3-based devices displayed a higher V_{OC} than MAPI. We also note a huge drop in V_{OC} and FF when going from BA3 to BA2. It should be also noted that the devices showed a relatively small hysteresis (**Figure 1 (a)**), which also facilitates the interpretation of the following optical and electrical measurements.

Table 1. Photovoltaic performance parameters including standard deviation and parameters of the best cells in brackets of ITO/PTAA/PFN-Br/Perovskite/C_{60}/BCP/Cu devices employing 3D MAPI and (Cs^+) doped 2D BA systems under AM1.5G illumination (~100 mWcm^{-2}).

Device	Voc (V)	Jsc (mA/cm^2)	FF (%)	PCE (%)
MAPI	1.08±0.02	23±0.4	0.75±0.02	18.7±0.6
($MAPbI_3$)	1.1	23	0.77	19.5
BA4	1.12±0.01	18.4±1.4	0.64±0.05	13.2±0.8
($BA_2MA_3Pb_4I_{13}$)	1.12	19.3	0.69	14.9
BA3	1.13±0.02	15.8±0.7	0.57±0.03	10.2±0.5
($BA_2MA_2Pb_3I_{10}$)	1.14	17.1	0.57	11.1
BA2	0.90±0.07	4.1±0.9	0.25±0.03	0.94±0.2
($BA_2MAPb_2I_7$)	0.95	5.5	0.27	1.4

In order to elucidate the loss mechanism responsible for the differences in device efficiency of these two-dimensional perovskites we first estimated the bandgaps (E_G) from the inflection point of the external quantum efficiency (EQE) as proposed by Kirchartz and Rau et al.[36,37] We obtained the following bandgaps: MAPI~1.61 eV, BA4~1.65 eV, BA3~1.71 eV and BA2~2.0 eV. Then, we quantified the Urbach energy (E_U) from the slope of the exponential EQE or absorption tail which is proportional to $\exp((E - E_G)/E_U)$ and we obtained 16 meV for MAPI, 18 meV for BA4, 20 meV for BA3 and 37 meV for BA2, comparable to

previous reports.[38] It is well established that the Urbach energy is related to structural disorder in the material, where a higher Urbach energy is indicative of more disorder. The sharpness of the band edge absorption implies direct optical transitions and a low density of sub-gap states in the 3D (MAPI) and the two-dimensional (BA4, BA3) systems, and hence the high quality of these crystalline materials. However, in the BA2 system, the absorption onset changed considerably with a broader sub-gap tail, which may be due to the structural and/or thermal disorder.[39],[40] In addition, sharp exciton peaks appear in the absorption spectra of the two-dimensional materials, and in the case of BA2 also in the EQE, which might be related to the enhanced confinement of charge carriers in the $[PbI_6]^{4-}$ octahedral sheets (**Figure 1(c)**).[24] The main feature for the BA4 system was at 2.0 eV and that for BA2 was at 2.18 eV. BA3 showed a combination of both BA2 and BA4 features indicating a potential mixture of the two. **Figure 1(d)** presents the predicted energy diagram obtained by combining the above bandgap analysis and measured ionization potentials of the perovskite films using photoelectron yield spectroscopy (PYS). From the diagram it can be seen that the ionization potentials of the 2D perovskite films are sufficiently similar such that in principle they should not affect the hole transfer to the anode. However, we note a large energy offset between the conduction bands of the 2D perovskites and the electron affinity (EA) of C_{60}, which suggests that the upward shift of the conduction band minimum for decreasing n does not translate into a comparable increase of the open-circuit voltage.[41],[42],[43]
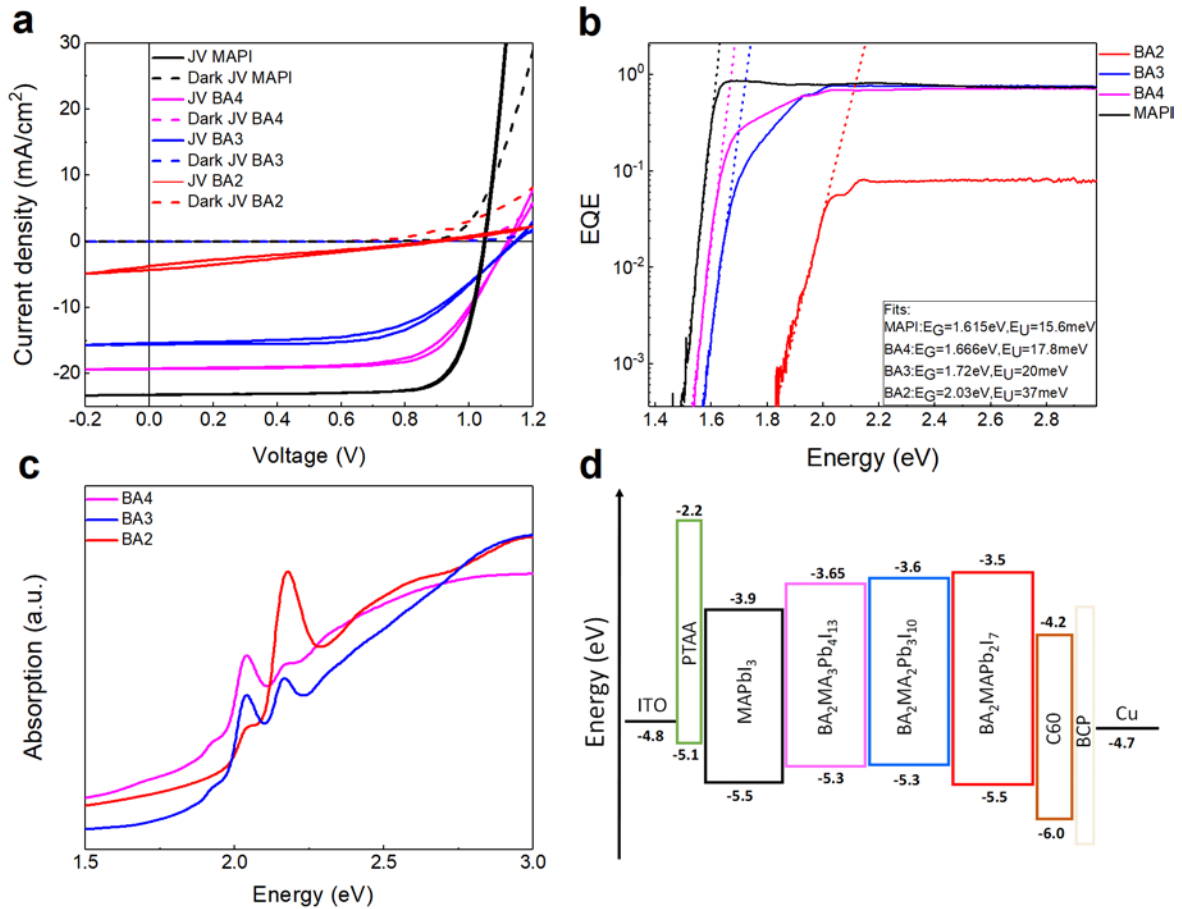
Figure 1. *Performance and electro-optical properties of the layered perovskites and MAPI. **(a)** Dark and light (forward-reverse) J-V curves of the best devices. **(b)** External Quantum Efficiencies (EQEs) and Urbach energies as obtained from exponential fits to the band edge of the EQEs. **(c)** UV-visible absorption spectra of the layered perovskites and **(d)** energy levels of the studied perovskites based on the ionization potential measured using photoelectron yield spectroscopy (PYS) and the optical gap.*

Structural investigation of layered perovskites using X-ray diffraction.

In order to unravel the orientation of the layered perovskites with respect to the substrate, we performed out-of-plane and in-plane X-ray diffraction, which allow probing of lattice planes that are parallel and perpendicular to the substrate, respectively. The XRD patterns obtained from these measurements are shown in **Figure 2(a-c)** and compared with calculated X-ray diffraction patterns in preferred and random orientation using the FullProf Suite software package.[44] For the pattern calculation, the structural models for the BA2 (space group Cc2m), BA3 (space group Acam) and BA4 (space group Cc2m) were employed.[45] **Figure 2(d)** displays the deduced orientations of each of the layered perovskites with respect to a flat substrate. Importantly, for BA2 we identified the 020 (and any other order = 0k0) plane (i.e., the $[PbI_6]^{4-}$ octahedral layers) being parallel to the substrate.[35,45] In contrast, for the BA3 and BA4 samples, the $[PbI_6]^{4-}$ layers (= 020 and higher orders (0k0) planes) are oriented almost normal (BA3 ~ 83°, BA4 ~ 85°) to the substrate, also consistent with literature.[35,45]
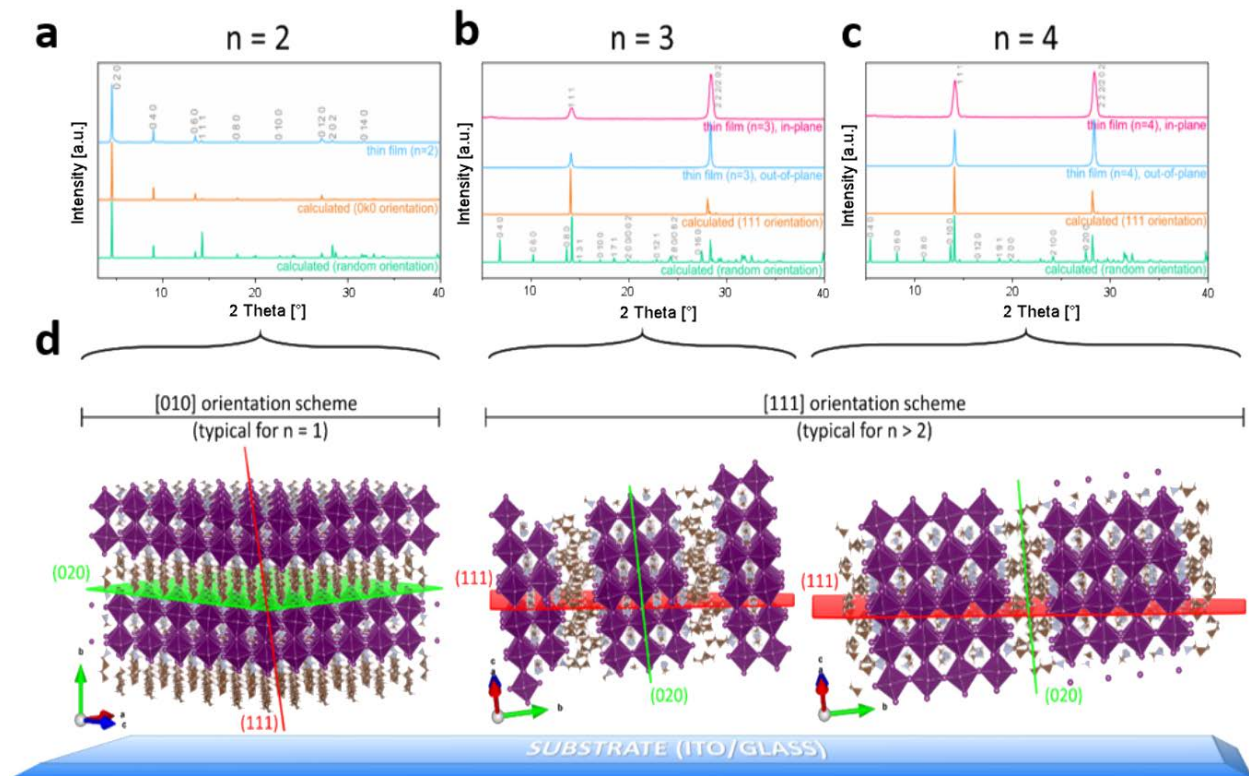
Figure 2. *X-ray Diffraction. Comparison between measured XRD patterns of (a) BA2, (b) BA3 and (c) BA4 Ruddlesden–Popper perovskite (RPP) thin film samples (blue = out-of-plane, red = in-plane) and calculated XRD patterns (green = random orientation, amber = preferred orientation along the [010] direction in the case of BA2 and along the [111] direction in the case of BA3 and BA4). (d) Schematics of the structure of n = 2-4 RPPs showing the change in periodicity between inorganic and organic layers that also strongly*

affects the dimension of the unit cell parameter b. The [PbI$_6$]$^{4-}$ layers are nearly perpendicular to the substrate in the case of BA3 and BA4 and parallel in the case of BA2 RPPs.

The appearance of the 111 and 202 reflections in the out-of-plane XRD pattern recorded for the BA2 films might be explained by the competing effects the *n*-butylammonium and the methyl ammonium molecules have on the growth properties as soon as *n* > 1[35]. Thus, while the general tendency of the BA2 materials to orient their layers parallel to the substrate can be clearly observed, this is partly accompanied by another orientation that is typical for the *n* > 2 compounds. For these compounds, the preferential growth occurs mainly along the $[\bar{1}2\bar{1}]$ direction resulting in 111 lattice planes being oriented parallel with respect to the substrate and, thus, fulfill the diffraction condition for out-of-plane geometry. From symmetry considerations, the 111 lattice planes can be also captured by in-plane XRD. In fact, both out-of-plane as well as in-plane measurements clearly revealed the two-dimensional nature of the BA3 and BA4 RPP thin film samples as only 111 lattice planes (and higher orders) are in the appropriate orientation to meet the diffraction condition. In addition, we recorded pole figures (**Supplementary Note 1** and **Supplementary Figure S2**) of certain peaks by tracking their intensity distribution along the phi and psi space, which confirmed the conclusions made from the out-of-plane and in-plane XRD measurements.

Charge carrier recombination and free energy losses

In the first step in studying the opto-electronic properties of the two-dimensional layered perovskites (and MAPI as a reference) we used TRPL to evaluate the time-dependent recombination kinetics in the bulk and interfaces under the same excitation fluences (~10 nJcm^{-2}). Several earlier studies demonstrated an increased radiative emission yield by tuning the ratio of small molecule components [MA:formamidinium (FA)] in the BA4 films[46] or by increasing the Cs$^+$ amount.[8] Qualitatively, **Figure 3(a)** shows that the TRPL decay time increases with increasing *n* while MAPI exhibits the longest TRPL decay lifetime. Generally, multicomponent TRPL decay dynamics were observed for the two-dimensional perovskite films, which indicates a combination of different recombination processes of different order. Addition of the HTL (PTAA/PFN-Br) was found to prolong the PL lifetime, which might indicate passivation of the glass/perovskite interface. **Figure 3(b)** shows the corresponding spectral photon emission under a 1 sun equivalent laser illumination (445 nm). Notably, addition of the HTL leads to an increased PL yield for the two-dimensional perovskite films. This confirms our conclusion from TRPL lifetime measurements that the addition of the PTAA/PFN-Br layer goes along with a passivation of recombination sites at the perovskite bottom surface. However, MAPI does not follow this trend, exhibiting the longest TRPL decay despite its PLQY being lower than for the BA4 and BA3 devices. This might indicate a higher second order recombination rate constant for the BA3 and BA4 films, which could potentially lead to a more rapid TRPL decay despite a higher steady-state PLQY than MAPI.
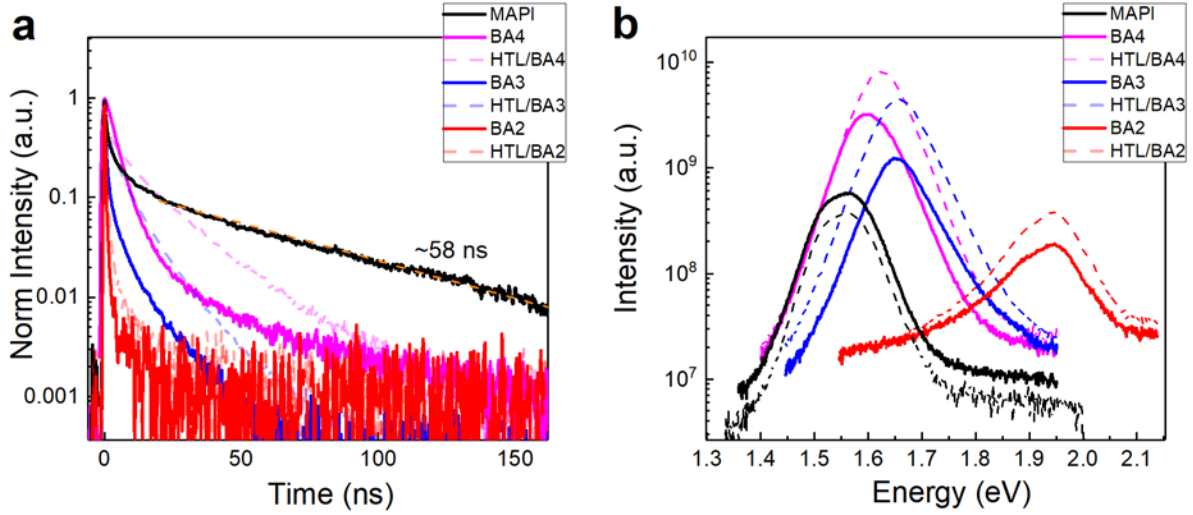
Figure 3. *Transient PL and steady state photoluminescence spectra of the BA- and MAPI-perovskite films.* *(a) TRPL of the two-dimensional BA-perovskite and MAPI films (solid lines) as well as the PTAA/PFN-Br/BA films (dashed lines). (b) Photoluminescence spectra of the BA-perovskite and MAPI films (solid lines) and the PTAA/PFN-Br/BA films (dashed lines) from absolute PLQY measurements.*

The PLQY can also be used to directly measure the quasi-Fermi level splitting (QFLS or μ) in the neat absorber layer or in the individual components of the multilayer device stack.[47],[48],[49],[50] In particular, comparing the QFLS in the absorber layer with and without the transport layers (TLs) allows quantification of the non-radiative losses at the perovskite/TL interfaces. Therefore, to disentangle the origin of non-radiative recombination losses in the devices we calculated the QFLS of the neat perovskite films, HTL/perovskite as well as *p-i-n* stacks using the following relation between the QFLS and the PLQY[47],[48] junctions,

$$\mu = kT \ln \left(\text{PLQY} \frac{J_G}{J_{0,\text{rad}}} \right)$$

(eq. 1)

While other methods are more commonly employed to calculate μ from the emitted photon flux, such as the high energy tail fit,[2],[51] equation 1 is very simple and less error-prone as it allows determination of μ from only four well-accessible parameters: 1) the temperature (T), which can be precisely measured on the sample during the measurement (we obtained $T \sim 26$ °C using an infrared sensor); 2) the generation current density (J_G), which is equal to the J_{SC} in almost all cases; 3) the radiative recombination current density in thermal equilibrium ($J_{0,\text{rad}}$), which is obtained from the overlap of the black body spectrum (at 300 K) and the measured EQE

$$J_{0,\text{rad}} = q \int EQE_{PV} \, \phi_{BB} (E) dE \ ,$$

(eq. 2)

and 4) the PLQY by

$$\text{PLQY} = \frac{\phi_{\text{em}}}{\phi_{\text{abs}}} = \frac{J_{\text{rad}}}{J_G} = \frac{J_{\text{rad}}}{J_{R,\text{tot}}} = \frac{J_{\text{rad}}}{J_{\text{rad}} + J_{\text{non-rad}}}$$

(eq. 3)

The obtained thermal radiative recombination current $J_{0,\mathrm{rad}}$ of MAPI and the layered perovskite films are shown in **Table 2**. Interestingly, while $J_{0,\mathrm{rad}}$ decreases from MAPI to BA3, it is highest for BA2 due to its broad absorption tail.

Table 2. Calculated dark radiative saturation currents ($J_{0,\mathrm{rad}}$) of the layered perovskites and MAPI.

	MAPI	BA4	BA3	BA2
$J_{0,\mathrm{rad}}$ (A/cm^2)	1.5e^{-20}	1.5e^{-21}	7.6e^{-22}	2.2e^{-20}

The PLQY equals the ratio of the emitted and absorbed photon fluxes ($\phi_{\mathrm{em}}/\phi_{\mathrm{abs}}$), or likewise the radiative and generation current densities $J_{\mathrm{rad}}/J_{\mathrm{G}}$. At V_{OC}, J_{G} also equals the total recombination current density ($J_{\mathrm{R,tot}}$), which is the sum of the radiative and non-radiative recombination currents ($J_{\mathrm{rad}} + J_{\mathrm{non-rad}}$). The measured PLQYs are summarized in **Table 3** together with the values of the quasi-Fermi level splitting of the films and devices (without metal contact). All the perovskite films exhibited radiative efficiencies on the order of 1×10^{-4} to 1×10^{-3}, with BA4 yielding the highest PLQY (1.8×10^{-3}), followed by BA3 (7.1×10^{-4}), MAPI (4.9×10^{-4}) and BA2 (1.1×10^{-4}). As suggested by the transient and steady state PL experiments in Figure 3, adding the PTAA(PFN-Br) materials generally increased the PLQY ($\approx$1.5 to 3 times), while addition of the C$_{60}$ ETL caused additional non-radiative recombination. Interestingly, despite different PLQYs of the neat perovskite, the complete *p-i-n*-stacks exhibited comparable radiative efficiencies of about (1.0-1.6)×10^{-4}, which suggests that non-radiative losses in the bulk and at interfaces contribute differently to the PLQY of the multilayer stacks for different *n*.

Table 3. The QFLS of all BA and MAPI neat films, PTAA(PFN-Br)/perovskite and PTAA(PFN-Br)/perovskite/C$_{60}$ "*p-i-n*-stacks" and the EQE_{EL} of complete devices. Also shown are the film absorption (Abs), PLQY and the electroluminescence quantum efficiency (EQE_{EL}) of the complete device.

Films on glass	Abs (%)	PLQY	EQE$_{\mathrm{EL}}$	QFLS (eV)
MAPbI3 (neat)	84.4	4.9×10^{-4}		1.122
PTAA(PFN-Br)/MAPbI3	84.6	4.0×10^{-4}		1.117
PTAA(PFN-Br)/MAPbI3/C$_{60}$	94.0	1.6×10^{-4}	8.1×10^{-5}	1.093
BA4 (neat)	83.9	1.8×10^{-3}		1.210
PTAA(PFN-Br)/BA4	83.5	4.0×10^{-3}		1.231
PTAA(PFN-Br)/BA4/C$_{60}$	94.2	1.0×10^{-4}	3.9×10^{-4}	1.135
BA3 (neat)	85.0	7.1×10^{-4}		1.199
PTAA(PFN-Br)/BA3	84.2	2.4×10^{-3}		1.230
PTAA(PFN-Br)/BA3/C$_{60}$	92.9	1.5×10^{-4}	7.6×10^{-5}	1.159
BA2 (neat)	86.2	1.1×10^{-4}		1.028
PTAA(PFN-Br)/BA2	86.2	1.8×10^{-4}		1.042
PTAA(PFN-Br)/BA2/C$_{60}$	93.7	1.2×10^{-4}	1.4×10^{-4}	1.032

Radiative and non-radiative recombination losses in the bulk,and at the interfaces and contacts

Based on data in **Table 3** we were able to identify how the different recombination current losses affect the QFLS and with that the achievable open-circuit voltage of the two-dimensional perovskite and MAPI films. The different QFLS-losses in the bulk (radiative and non-radiative), at the perovskite/TL interfaces and additional losses due to the presence of the electrodes are plotted in **Figure 4**. The blue hexagons in **Figure 4** show the QFLS in the perovskite bulk as obtained from **equation 1**. In order to quantify the non-radiative recombination losses in the absorber layer, we first calculated the achievable QFLS in the radiative limit (QFLS$_{rad}$) where the PLQY = 1, which is shown in **Figure 4** by the blue circles. Accordingly, the difference between the blue circles and hexagons highlights the free energy losses in the perovskite bulk due to non-radiative recombination, which we assign to Shockley-Read-Hall (SRH) recombination. Consistent with the PLQY of the neat films, the lowest non-radiative recombination loss in the bulk was found for BA4 ($\sim$165 mV), followed by BA3 ($\sim$191 mV), MAPI ($\sim$199 mV) and BA2 ($\sim$245mV). Notably, the loss in BA4 is approximately 34 mV less than the loss in MAPI. This suggests a comparatively low density of defects in the layered perovskites, or if most losses happen at the perovskite surface, that the inclusion of BA ions reduces the probability of photogenerated charges reaching the surface. In order to compare the non-radiative to radiative recombination losses in the perovskite bulk, we quantified the maximum QFLS (QFLS$_{S.Q.}$) that could be theoretically achieved for a given bandgap, which is known as the detailed-balance (or thermodynamic) limit according to Shockley and Queisser.[52] The model considers the solar cell as a black body that emits as much radiation as it absorbs in thermodynamic equilibrium with its surrounding. QFLS$_{S.Q}$ is then obtained in the limit of step-wise device absorption, where the absorption is 0 below the bandgap and 1 above (which results in a lower limit of $J_{0,\mathrm{rad}}$). This maximum voltage is displayed in **Figure 4** by the red points, where the difference to the blue circles highlights the radiative recombination losses in the cells. Interestingly, while the V_{OC} loss is dominated by non-radiative recombination in MAPI and the layered perovskites BA3 and BA4, in BA2, the radiative voltage loss outweighs the non-radiative voltage loss.

In order to quantify the non-radiative recombination loss at the perovskite/TL interfaces we compared the QFLS of the neat materials with the QFLS of HTL/perovskite and HTL/perovskite/electron extraction layer (ETL) junctions. As already mentioned above, we observe an increase in PLQY ($\approx$1.5 to 3 times) relative to the neat materials when the two-dimensional materials (not in case of MAPI) were deposited onto the PTAA:PFN-Br layer, demonstrating the passivating effect of the PTAA/PFN-Br at the *p*-interface with respect to glass/perovskite. However, for the complete *p-i-n*-stacks, **Table 3** shows that the PLQY is considerably reduced for all the films with respect to the HTL/perovskite junctions ($\sim$2.5x in case of MAPI, $\sim$16x in case of BA3 and $\sim$40x in BA4), except for the BA2 system where we observe almost no changes in the PLQY upon addition of any interlayer. Thus, we can conclude that significant recombination losses occur at the perovskite/ETL interface except for the BA2 system. The differences between the blue hexagons and the green diamonds (i.e., the QFLS of the neat materials and the *p-i-n*-stacks) highlights the *additional* V_{OC} losses due to the addition of both TLs. It is important to note that, although the additional voltage losses due to non-radiative interfacial recombination are overall smaller than the voltage losses due to recombination in the bulk, the interfacial recombination current still outweighs the recombination current in the bulk for MAPI, BA3 and BA4.[47]
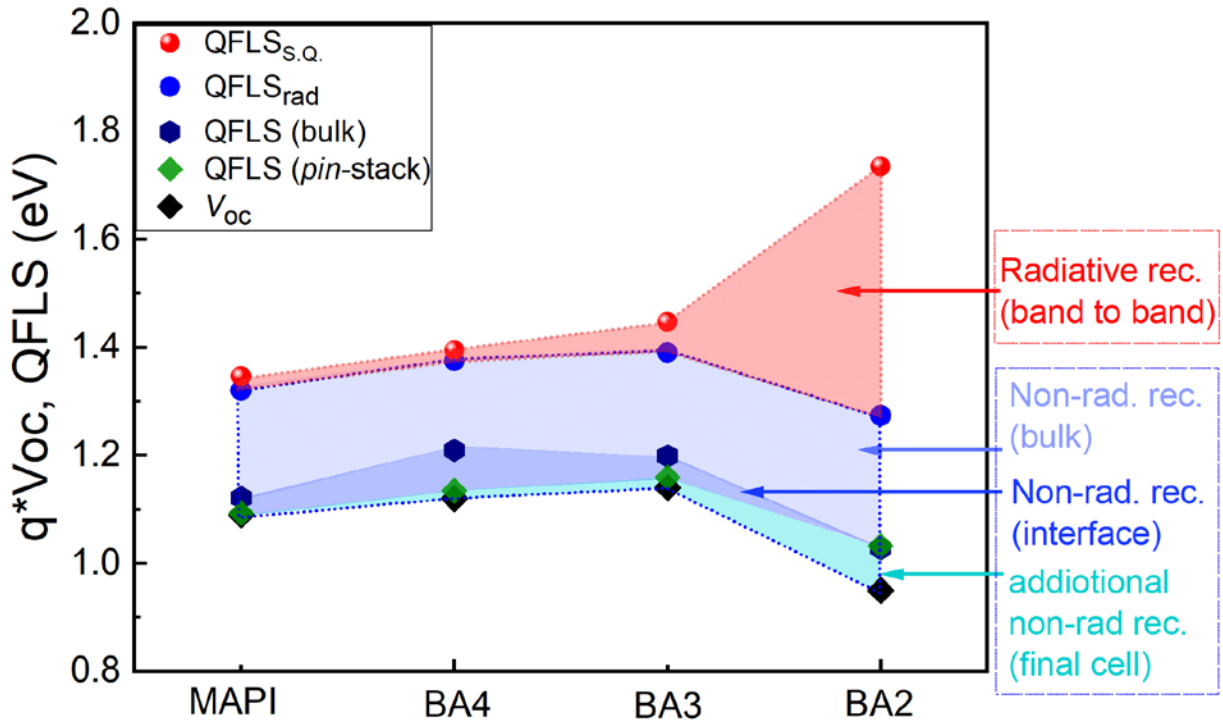
Figure 4. *QFLS and Voc losses in the bulk, and at the interfaces and electrodes*. *The QFLS obtained in the bulk of the layered perovskites and MAPI (blue hexagons) is impacted by radiative (red shaded area) and non-radiative (light blue shaded area) recombination losses, while the QFLS in the p-i-n-stacks (green diamonds) is affected by additional non-radiative interfacial recombination losses (blue shaded area). The presence of the electrodes in the final cell causes addional non-radiative recombination losses with respect to the QFLS of the p-i-n-stack (turquoise shaded area).*

It is also important to note that the QFLS of the *p-i-n*-stacks fits very well with the measured qV_{OC} of the MAPI, BA3 and BA4 cells. In contrast to this, there is a rather considerable mismatch between these two parameters (~90 meV) in the case of the BA2 device. As we demonstrated in a recent study,[43] a matched internal and external QFLS (i.e., qV_{OC}) indicates a flat QFLS throughout the multilayer device stack and also suggests that the presence of the metal contacts is not causing substantial additional recombination losses. A mismatched QFLS-V_{OC} on the other hand, may be caused by a considerable majority carrier band offset, namely between the perovskite conduction (valence) band and the electron affinity (ionization potential) of the electron (hole) selective TL, respectively. In such cases, the electron or hole quasi-Fermi level bends towards the TL or the contact, which causes a larger internal QFLS compared to the splitting at the metal contacts. Considering the energy levels obtained from PYS (**Figure 1(a)**), it appears that there is indeed a large band offset for electrons in the case of BA2, which is likely to cause the observed difference between the QFLS and the V_{OC}. Lastly, we also performed electroluminescence measurements in order to check the device V_{OC}, which can be calculated based on Rau's reciprocity[53] by using the experimentally measured

EQE_{EL} (see **Table 3**) instead of the PLQY in **equation 1**. The corresponding measurements are shown in **Supplementary Figure S3**, which demonstrate that under conditions where the dark injected dark current matches J_G (under 1-sun), the $V_{OC,EL}$ matches more closely the QFLS of the *p-i-n*-stack than the device V_{OC}.

Charge transport losses in the two-dimensional perovskites

While the previous section shed light on the origin of radiative and different non-radiative recombination pathways in determining the open-circuit voltage of the layered perovskites and MAPI, the difference in their performance was largely a result of their different FFs (**Figure 5(a)**). This is a common observation when comparing solar cells from layered perovskites to their 3D counterparts. In order to unravel the processes behind these losses, we employed IPC measurements.[32,33] In this experiment, the photocurrent (i.e., the current measured under illumination minus the dark current) increases linearly with light intensity until second-order bimolecular recombination with regard to the light intensity becomes significant compared to the extraction rate (i.e., $E \sim R$) which causes the photocurrent to deviate from linearity. To visualize the onset of these second-order recombination losses we plot the normalized EQE as a function of the photocurrent of the device, which was increased using a CW laser at an excitation wavelength of 445 nm (**Figure 5(b)**). The EQE is flat until approximately ~50 suns for the MAPI and BA4 solar cells, which demonstrates the absence of significant second-order recombination losses as was previously observed for triple cation perovskite solar cells.[29] However, in the cases of BA3 and BA2, considerable bimolecular losses appear at much lower photocurrents and light intensities. While the onset of the EQE decrease happens at intensities >1 sun for the BA3 cell, in the case of BA2 the short-circuit current (at 1 sun) is already strongly limited by bimolecular recombination. We have previously shown that the limiting photocurrent at the onset of the recombination losses is proportional to the slower carrier mobility[54,55] as the charge carrier density increases inversely with the mobility for a given photocurrent at a bias of 0 V. Thus, the IPC results strongly suggest a substantial slowing of charge extraction in the layered perovskites from MAPI to BA4 to BA3 and in particularly in the BA2 system where the $[PbI_6]^{4-}$ octahedral layer orientate parallel to the substrate. Notably, this is also consistent with integral time of flight transients shown in **Figure 5(c)** that demonstrate a much slower charge extraction time in the BA2 device (~10 µs) compared to the BA3 where a large majority of photo-generated charge was extracted after 30 ns. The corresponding transients for MAPI and BA4 are shown in **Supplementary Figure S4**, which likewise show fast extraction from the device at the limit of the temporal response of the setup (refer to the **Supplementary Methods** for further details).

Finally, given the excitonic nature of the BA2 system, we also studied the efficiency of free charge generation in the two-dimensional system using time delayed collection field-experiments (TDCF).[34] In essence, TDCF allows assessment of the populations of free charges prior to their recombination. The cell is held at a variable pre-bias (for several ms) during which a ns-pulsed laser (532 nm with low fluences around 0.02 µJ/cm^2) creates charges in the cell. After a short-delay-time, these charges are extracted with a reverse bias (-0.5V). In combination with a short delay time (~5 ns), free charge recombination can be reduced and the total extracted charge gives the initially generated carrier density. This is seen by the fact that the extracted charge saturates with decreasing delay time. **Figure 5(d)** shows the *JV* and corresponding EQE versus carrier density (which we call the external generation efficiency, EGE) at a delay time of 6 ns as a function of the pre-bias. The nearly flat EGE in the layered perovskites indicates that charge generation was not field-dependent, not even for the BA2 cells. This was also consistent with the EQE spectrum of the BA2 devices where the spectral shape (including its excitonic features) is nearly independent on the pre-bias (**Supplementary Figure S5**). Overall, these experiments further support the

asserton that the FF of these layered perovskite suffers primarily from inefficient free charge collection as opposed to field-dependent exciton recombination.
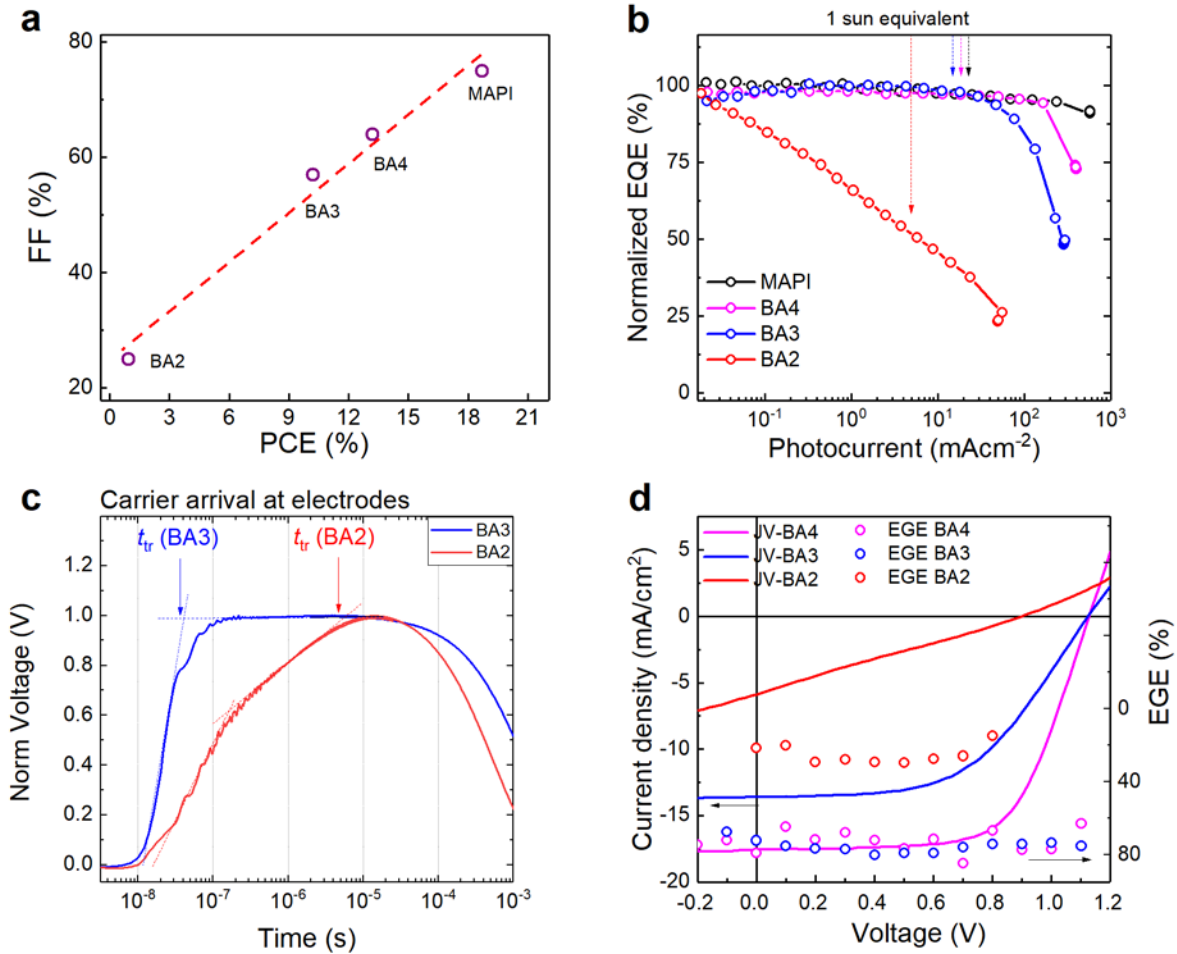

Figure 5. *Charge transport in two-dimensional perovskite.* *(a) The fill factor (FF) versus power conversion efficiency highlights the impact of the FF on the photovoltaic performance of the BA-based two-dimensional perovskite and MAPI cells. (b) The normalized external quantum efficiency (EQE) at 445 nm and short-circuit conditions as a function of the device photocurrent (light minus dark current), which was increased using the applied laser power. The photocurrent at which the EQE starts to decrease is proportional to the mobility of the slowest charges in the device, which highlights the large decrease in the extraction efficiency with decreasing number of [PbI$_6$]$^{4-}$ layers (MAPI > BA4 > BA3 > BA2). The arrows mark the 1-sun short-circuit current density, which highlight the substantial bimolecular recombination losses in BA2. (c) Integral time of flight transients measured on BA3 and BA2 cells at a bias of 0 V, a load resistance of 1 MΩ after a ns laser excitation. The large resistance–capacitance (RC) time of the external circuit allows visualization of the displacement of photogenerated charges within the active layer and consequently the saturation of the photovoltage signal marks the transit time (t$_{tr}$) of all photogenerated charges through the device (30 ns and ~10 μs for BA3 and BA3, respectively). (d) Field dependence of free charge generation*

13

of the BA perovskites as measured using time-delayed collection field experiments. The results suggest field-independent charge generation in the layered perovskite film devices.

Conclusion:

This work demonstrates how different recombination processes determine the open-circuit voltage and the FF of two-dimensional perovskites in comparison to MAPI. In the first part, transient and absolute PL measurements were applied to investigate the radiative and non-radiative recombination loss mechanisms in the bulk perovskite absorbing layers and at the interfaces. While radiative recombination was found to be negligible compared to non-radiative recombination in the BA4, BA3 and MAPI films, in the BA2 system, radiative recombination was a major V_{OC} loss mechanism due to its broad Urbach tail. Interestingly, the bulk BA4 and BA3 films exhibited a higher PLQY than MAPI and BA2, and by selecting PTAA/PFN-Br as a hole extraction interlayer, the HTL/perovskite interface was largely passivated, allowing V_{OC}s as high as $\sim$1.23 V to be achieved. However, the PLQY of the *p-i-n*-stacks were very similar ($\sim$1x10^{-4}), even in the BA2 system, which points to the importance of the perovskite/C_{60} interface in determining the open-circuit voltage of these BA-based two-dimensional perovskites in a *p-i-n*-configuration. Moreover, the QFLS of the *p-i-n* stack as calculated from the PLQY was almost identical to the device V_{OC} in all cases, again with the exception of the BA2 system where the internal QFLS was $\sim$90 meV higher than the device V_{OC}. The result for the BA2 cell indicates a bending of the Fermi levels towards the electrodes, which leads to QFLS > qV_{OC}. Lastly, the origin behind the FF losses were studied. Intensity dependent photocurrent and integral TOF measurements highlighted the significant charge collection issues in the BA2 systems where the $[PbI_6]^{4-}$ units were oriented parallel to the substrate. Moreover, TDCF and bias dependent EQE measurements indicate field-independent charge generation in all the cells. Therefore, the FFs of these layered perovskite suffers primarily from inefficient charge extraction as opposed to bias dependent exciton recombination. Overall, this work suggests that vertically aligned $[PbI_6]^{4-}$ layers are necessary to reach efficient and stable two-dimensional perovskite films and that significant performance improvements will be possible through suppression of non-radiative recombination at the interfaces and in the absorber layer.

References:

[1]   NREL, "Best Research-Cell Efficiencies," can be found under
        https://www.nrel.gov/pv/assets/pdfs/pv-efficiency-chart.20190103.pdf, **2019**.

[2]   I. L. Braly, D. W. DeQuilettes, L. M. Pazos-Outón, S. Burke, M. E. Ziffer, D. S. Ginger, H. W.
        Hillhouse, *Nat. Photonics* **2018**, *12*, 355.

[3]   Q. Fu, X. Tang, B. Huang, T. Hu, L. Tan, L. Chen, Y. Chen, *Adv. Sci.* **2018**, *5*, 1.

[4]   Z. Liang, K. Tang, Q. Shao, G. Li, S. Zeng, H. Zheng, *J. Solid State Chem.* **2008**, *181*, 964.

[5]   S. N. Ruddlesden, P. Popper, *Acta Crystallogr.* **1957**, *10*, 538.

[6]   I. C. Smith, E. T. Hoke, D. Solis-Ibarra, M. D. McGehee, H. I. Karunadasa, *Angew. Chemie - Int. Ed.*
        2014, *53*, 11232.

[7]   H. Tsai, W. Nie, J. C. Blancon, C. C. Stoumpos, R. Asadpour, B. Harutyunyan, A. J. Neukirch, R.
        Verduzco, J. J. Crochet, S. Tretiak, L. Pedesseau, J. Even, M. A. Alam, G. Gupta, J. Lou, P. M. Ajayan,
        M. J. Bedzyk, M. G. Kanatzidis, A. D. Mohite, *Nature* **2016**, *536*, 312.

[8]   X. Zhang, X. Ren, B. Liu, R. Munir, X. Zhu, D. Yang, J. Li, Y. Liu, D. Smilgies, R. Li, Z. Yang, T. Niu, X.
        Wang, A. Amassian, K. Zhao, S. F. Liu, *Energy Environ. Sci.* **2017**, *10*, 2095.

[9]   H. Lai, B. Kan, T. Liu, N. Zheng, Z. Xie, T. Zhou, X. Wan, X. Zhang, Y. Liu, Y. Chen, *J. Am. Chem. Soc.*
        2018, *140*, 11639.

[10]   Y. Bai, S. Xiao, C. Hu, T. Zhang, X. Meng, H. Lin, Y. Yang, S. Yang, *Adv. Energy Mater.* **2017**, *7*, 1.

[11]   C. Ma, C. Leng, Y. Ji, X. Wei, K. Sun, L. Tang, J. Yang, W. Luo, C. Li, Y. Deng, S. Feng, J. Shen, S. Lu, C.
        Du, H. Shi, *Nanoscale* **2016**, *8*, 18309.

[12]   K. T. Cho, G. Grancini, Y. Lee, E. Oveisi, J. Ryu, O. Almora, M. Tschumi, P. A. Schouwink, G. Seo, S.
        Heo, J. Park, J. Jang, S. Paek, G. Garcia-Belmonte, M. K. Nazeeruddin, *Energy Environ. Sci.* **2018**,
        11, 952.

[13]   G. Grancini, C. Roldán-Carmona, I. Zimmermann, E. Mosconi, X. Lee, D. Martineau, S. Narbey, F.
        Oswald, F. De Angelis, M. Graetzel, M. K. Nazeeruddin, *Nat. Commun.* **2017**, *8*, 1.

[14]   J. A. Sichert, Y. Tong, N. Mutz, M. Vollmer, S. Fischer, K. Z. Milowska, R. García Cortadella, B.
        Nickel, C. Cardenas-Daw, J. K. Stolarczyk, A. S. Urban, J. Feldmann, *Nano Lett.* **2015**,
        150903104944005.

[15]   V. A. Hintermayr, A. F. Richter, F. Ehrat, M. Döblinger, W. Vanderlinden, J. A. Sichert, Y. Tong, L.
        Polavarapu, J. Feldmann, A. S. Urban, *Adv. Mater.* **2016**, *28*, 9478.

[16]   Q. Wang, X.-D. Liu, Y.-H. Qiu, K. Chen, L. Zhou, Q.-Q. Wang, *AIP Adv.* **2018**, *8*, 025108.

[17]   Y. Tong, F. Ehrat, W. Vanderlinden, C. Cardenas-Daw, J. K. Stolarczyk, L. Polavarapu, A. S. Urban,
        ACS Nano **2016**, *10*, 10936.

[18]   X. Yang, X. Zhang, J. Deng, Z. Chu, Q. Jiang, J. Meng, P. Wang, L. Zhang, Z. Yin, J. You, *Nat.
        Commun.* **n.d.**, *9*, 570.

[19]   G.-C. X. A. W. H. Guo, JIA, Ze-jiao Shi, Ying-GONG Xia, QI WEI, YONG-HUA CHEN, **2018**, *26*, 66.

[20] D. Liang, Y. Peng, Y. Fu, M. J. Shearer, J. Zhang, J. Zhai, *ACS Nano* **2016**, *10*, 6897.

[21] J. Byun, H. Cho, C. Wolf, M. Jang, A. Sadhanala, R. H. Friend, H. Yang, T. W. Lee, *Adv. Mater.* **2016**, *28*, 7515.

[22] K. Zheng, Y. Chen, Y. Sun, J. Chen, P. Chábera, R. Schaller, M. J. Al-Marri, S. E. Canton, Z. Liang, T. Pullerits, *J. Mater. Chem. A* **2018**, *6*, 6244.

[23] J. Liu, J. Leng, K. Wu, J. Zhang, S. Jin, *J. Am. Chem. Soc.* **2017**, *139*, 1432.

[24] J. C. Blancon, H. Tsai, W. Nie, C. C. Stoumpos, L. Pedesseau, C. Katan, M. Kepenekian, C. M. M. Soe, K. Appavoo, M. Y. Sfeir, S. Tretiak, P. M. Ajayan, M. G. Kanatzidis, J. Even, J. J. Crochet, A. D. Mohite, *Science* **2017**, *355*, 1288.

[25] G. Xing, B. Wu, X. Wu, M. Li, B. Du, Q. Wei, J. Guo, E. K. L. Yeow, T. C. Sum, W. Huang, *Nat. Commun.* **2017**, *8*, DOI 10.1038/ncomms14558.

[26] R. L. Milot, R. J. Sutton, G. E. Eperon, A. A. Haghighirad, J. Martinez Hardigree, L. Miranda, H. J. Snaith, M. B. Johnston, L. M. Herz, *Nano Lett.* **2016**, *16*, 7001.

[27] X. Wu, M. T. Trinh, X. Y. Zhu, *J. Phys. Chem. C* **2015**, *119*, 14714.

[28] L. R. Perovskites, L. N. Quan, M. Yuan, R. Comin, O. Voznyy, E. M. Beauregard, S. Hoogland, A. Buin, A. R. Kirmani, K. Zhao, A. Amassian, D. H. Kim, E. H. Sargent, **2016**, DOI 10.1021/jacs.5b11740.

[29] M. Stolterfoht, C. M. Wolff, Y. Amir, A. Paulke, L. Perdigón-Toro, P. Caprioglio, D. Neher, *Energy Environ. Sci.* **2017**, *10*, 1530.

[30] X. Zhao, L. Tao, H. Li, W. Huang, P. Sun, J. Liu, S. Liu, Q. Sun, Z. Cui, L. Sun, Y. Shen, Y. Yang, M. Wang, *Nano Lett.* **2018**, *18(4)*, 2442.

[31] S. Shao, J. Liu, H. Fang, L. Qiu, G. H. Brink, J. C. Hummelen, L. J. A. Koster, M. A. Loi, *Adv. Energy Mater.* **2017**, *7*, 1701305.

[32] M. Stolterfoht, A. Armin, S. Shoaee, I. Kassal, P. Burn, P. Meredith, *Nat Commun* **2016**, *7*, DOI 10.1038/ncomms11944.

[33] M. Stolterfoht, S. Shoaee, A. Armin, H. Jin, I. Kassal, W. Jiang, P. Burn, P. Meredith, *Adv. Energy Mater.* **2017**, *7*, 1601379.

[34] S. Albrecht, W. Schindler, J. Kurpiers, J. Kniepert, J. C. Blakesley, I. Dumsch, S. Allard, K. Fostiropoulos, U. Scherf, D. Neher, *J. Phys. Chem. Lett.* **2012**, *3*, 640.

[35] D. H. Cao, C. C. Stoumpos, O. K. Farha, J. T. Hupp, M. G. Kanatzidis, *J. Am. Chem. Soc.* **2015**, *137*, 7843.

[36] U. Rau, B. Blank, T. C. M. Müller, T. Kirchartz, *Phys. Rev. Appl.* **2017**, *7*, 1.

[37] T. Kirchartz, U. Rau, *Adv. Energy Mater.* **2018**, *1703385*, DOI 10.1002/aenm.201703385.

[38] W. Tress, *Adv. Energy Mater.* **2017**, *7*, 1602358.

[39] C. C. Stoumpos, C. M. M. Soe, H. Tsai, W. Nie, J. C. Blancon, D. H. Cao, F. Liu, B. Traoré, C. Katan, J. Even, A. D. Mohite, M. G. Kanatzidis, *Chem* **2017**, *2*, 427.

[40] X. Wu, M. T. Trinh, D. Niesner, H. Zhu, Z. Norman, J. S. Owen, O. Yaffe, B. J. Kudisch, X. Y. Zhu, *J. Am. Chem. Soc.* **2015**, *137*, 2089.

[41] L. E. Polander, P. Pahner, M. Schwarze, M. Saalfrank, C. Koerner, K. Leo, *APL Mater.* **2014**, *2*, 1.

[42] P. Schulz, E. Edri, S. Kirmayer, G. Hodes, D. Cahen, A. Kahn, *Energy Environ. Sci.* **2014**, *7*, 1377.

[43] M. Stolterfoht, P. Caprioglio, C. M. Wolff, J. A. Márquez, J. Nordmann, S. Zhang, D. Rothhart, U. Hörmann, A. Redinger, L. Kegelmann, S. Albrecht, T. Kirchartz, M. Saliba, T. Unold, D. Neher, *under Consid. Energy Enviromental Sci. "Preprint http//arxiv.org/abs/1810.01333"* **2018**.

[44] J. Rodríguez-carvajal, L. L. B. Cea-cnrs, C. E. A. Saclay, Y. Cedex, **2014**.

[45] C. C. Stoumpos, D. H. Cao, D. J. Clark, J. Young, J. M. Rondinelli, J. I. Jang, J. T. Hupp, M. G. Kanatzidis, *Chem. Mater.* **2016**, *28*, 2852.

[46] N. Zhou, Y. Shen, L. Li, S. Tan, N. Liu, G. Zheng, Q. Chen, H. Zhou, *J. Am. Chem. Soc.* **2018**, *140*, 459.

[47] M. Stolterfoht, C. M. Wolff, J. A. Márquez, S. Zhang, C. J. Hages, D. Rothhardt, S. Albrecht, P. L. Burn, P. Meredith, T. Unold, D. Neher, *Nat. Energy* **2018**, *3*, 847.

[48] V. Sarritzu, N. Sestu, D. Marongiu, X. Chang, S. Masi, A. Rizzo, S. Colella, F. Quochi, M. Saba, A. Mura, G. Bongiovanni, *Sci. Rep.* **2017**, *7*, 44629.

[49] I. L. Braly, H. W. Hillhouse, *J. Phys. Chem. C* **2016**, *120*, 893.

[50] G. El-Hajje, C. Momblona, L. Gil-Escrig, J. Ávila, T. Guillemot, J.-F. Guillemoles, M. Sessolo, H. J. Bolink, L. Lombez, *Energy Environ. Sci.* **2016**, *9*, 2286.

[51] G. H. Bauer, R. Brüggemann, S. Tardon, S. Vignoli, R. Kniese, *Thin Solid Films* **2005**, *480–481*, 410.

[52] W. Shockley, H. J. Queisser, *J. Appl. Phys.* **1961**, *32*, 510.

[53] T. Kirchartz, U. Rau, *Phys. Status Solidi Appl. Mater. Sci.* **2008**, *205*, 2737.

[54] M. Stolterfoht, A. Armin, B. Philippa, R. D. White, P. L. Burn, P. Meredith, G. Juška, A. Pivrikas, *Sci. Rep.* **2015**, *5*, 9949.

[55] M. Stolterfoht, A. Armin, B. Philippa, D. Neher, *J. Phys. Chem. Lett.* **2016**, *7*, 4716.

The role of bulk and interface recombination in high efficiency low dimensional perovskite solar cells

Shanshan Zhang[1,2], Seyed M. Hosseini[1], René Gunder[3], Andrei Petsiuk[3], Pietro Caprioglio[1], Christian M. Wolff[1], Safa Shoaee[1], Paul Meredith[4], Susan Schorr[3], Thomas Unold[3], Paul L. Burn[2], Dieter Neher[1], Martin Stolterfoht[1,*]

[1]Institute of Physics and Astronomy, University of Potsdam, Karl-Liebknecht-Str. 24-25, D-14476 Potsdam-Golm, Germany

[2]Centre for Organic Photonics & Electronics (COPE), School of Chemistry and Molecular Biosciences, The University of Queensland, Brisbane 4072, Australia

[3]Department of Structure and Dynamics of Energy Materials, Helmholtz-Zentrum-Berlin, Hahn-Meitner-Platz 1, D-14109 Berlin, Germany

[4]Department of Physics, Swansea University, Singleton Park, Swansea SA2 8PP Wales, United Kingdom

E-mail: stolterf@uni-potsdam.de

Supplementary Methods:

Materials preparation: PTAA (Sigma-Aldrich) was dissolved in toluene at a concentration of 1.5 mg/mL and spin-coated at 6000 rpm for 35 s. After 10 min annealing on a hotplate at 100 °C, the films were cooled down to room temperature and a 60 µL solution of PFN-Br (1-Material, 0.5 mg/mL in methanol) was deposited onto PTAA while the substrate was being spun at 5000 rpm for 20 s resulting in a film with thickness below the detection limit of our AFM (< 5 nm). To deposit the BA layered perovskite films, the 0.3 M precursor of MAI was mixed with BAI and PbI_2 with a molar ratio of 3:2:4 (BA4), 2:2:3 (BA3) and 1:2:2 (BA2) and 5 wt% CsI were dissolved in 1 mL of DMSO:DMF (7:3), respectively (ref.[8] main text). The solutions were stirred overnight in a nitrogen-filled glovebox. Then the films were quickly spin-coated on a hot glass substrates (100 °C) at 5,000 r.p.m for 30 s and annealed at 100 °C for 5 min on a hot plate. MAPI films were prepared by the one-step toluene assisted solution process. 100 uL of toluene was added dropwise at 40 s. The transparent perovskite film was then annealed at 100 °C for 5 min on a hot plate. All devices were completed by transferring the samples to an evaporation chamber where 30 nm C_{60}, 8 nm BCP (bathocuproine) (Sigma-Aldrich) and 100 nm copper (Sigma-Aldrich) at a rate of 0.6 Å/s were deposited under vacuum (p = 10^{-7} mbar).

Current density-voltage characteristics: JV-curves were obtained in a 2-wire source-sense configuration with a Keithley 2400. An Oriel class AAA Xenon lamp-based solar simulator was used for illumination providing approximately 100 mW cm^{-2} of AM1.5G irradiation and the intensity was monitored simultaneously with a Si photodiode. The exact illumination intensity was used for efficiency calculations, and the simulator was calibrated with a KG5 filtered silicon solar cell (certified by Fraunhofer ISE). During the JV-scan the devices were held at 25 °C room temperature using a Peltier element.

Absolute photoluminescence imaging: Excitation for the PL imaging measurements was performed with a 445nm CW laser (Insaneware) through an optical fiber into an integrating sphere. The intensity of the laser was adjusted to a 1 sun equivalent intensity by illuminating a 1 cm^2-size perovskite solar cell under short-circuit and matching the current density to the J_{SC} under the solar simulator (22.0 mA/cm^2 at 100 mWcm^{-2}, or 1.375x10^{21} photons m^{-2}s^{-1}). A second optical fiber was used from the output of the integrating sphere to an Andor SR393i-B spectrometer equipped with a silicon CCD camera/DU420A-BR-DD, iDus). The system was calibrated by using a calibrated Xe lamp with specified spectral irradiance, which was connected to an integrating sphere. A spectral correction factor was established to match the spectral output of the detector to the calibrated spectral irradiance of the lamp. The spectral photon density was obtained from the corrected detector signal (spectral irradiance) by division through the photon energy (hf), and the photon numbers of the excitation and emission obtained from numerical integration using Matlab. In a last step, three fluorescent test samples with high specified PLQY ($\sim$70%) supplied by Hamamatsu Photonics were measured where the specified value could be accurately reproduced within a relative error of less than 5%.

Electroluminescence: Absolute EL was measured with a calibrated Si photodetector (Newport) connected to a Keithley 485 pico Ampere meter. The detector (with active area of ~2 cm^2) was placed directly in front of the device (< 0.5 cm) and the total photon flux was evaluated considering the emission spectrum of the solar cell and the external quantum efficiency of the detector (around 86 % in the relevant spectral regime). A forward bias was applied to the cell using a Keithley 2400 source-meter and the injected current was monitored. Measurements were conducted with a home written LabVIEW routine. Typically, the voltage step was 20 mV and the current stabilized for 1 s at each step. No relevant changes in the EQE_{EL} were observed for different stabilization times.

Light intensity dependent measurements: Steady-state intensity dependent photocurrent and V_{OC} measurements were obtained with a 445 nm continuous wave laser (Insaneware) providing a power of 1

W. Two continuously variable neutral density filterwheels (ThorLabs) were used to attenuate the laser power. The photocurrent transients were recorded with a Keithley 2400 source measure unit. In order to measure the IPC at the specified voltages in forward bias we ensured a stabilized dark current, after typically tens of seconds (we note the stabilization time increased with increasing forward bias). The IPC responses in forward bias were then corrected by subtracting the dark (injection) current after the dark current stabilized. Each measured data point corresponds to a steady-state photocurrent measurement at the respective incident laser power and the steady-state conditions were assured by recording the temporal evolution of the photocurrent. The current output of a Silicon photodetector was simultaneously measured (Keithley 485) to improve the accuracy of the measurement. The EQE was obtained from the ratio of the photocurrent and the current output of the Si photodiode. In the V_{oc} -suns measurements we observe that the V_{oc} saturates to a maximum value at intensities >> 1 sun.

Integrated Time of Flight: Photovoltage transients were recorded with an oscilloscope (Agilent 81150A) at different external load resistances (R_{Load}) ranging up to 1 MΩ. A Q-switched neodymium-doped yttrium aluminum garnet (Nd:YAG) laser (NT242, EKSPLA)) with a pulse length of 5 ns and excitation wavelength of 532 nm was used to generate the charge carriers, while neutral optical density (OD) filters were used to attenuate the power output. The laser fluence was varied (resulting in a photovoltages between 50 mV to 100 mV at an R_{Load} of 1 MΩ) but kept significantly below the open-curcuit voltage to avoid significant field screening effects. The measurements were performed at a repetition rate of 10 Hz and showed no difference when compared with the single shot transients. We note the temporal response of the setup is limited to ~30 ns (which is similar to the observed response time of MAPI, BA4 and BA3) due to parasitic cable resistances and the finite laser pulse length. Thus, the obtained transit time in these three systems might be considered as an upper limit. In the case of BA2, the finite RC discharging time competes with the internal charging of the metal electrodes and the absence of a clear voltage saturation indicates that the extraction is not completed before the external discharge happens. Thus, the specified transit time for BA2 should be considered as a lower limit.

TDCF: In the TDCF experiments, laser pulses from a diode pumped, Q-switched Nd:YAG laser (NT242, EKSPLA) with 6 ns pulse duration and a typical repetition rate of 500 Hz were used to generate charges in the device. This charge generation was realized at different applied pre-voltages, Vpre. After a variable delay, a high reverse bias, Vcoll, was applied to extract all the charges in the device. A pulse generator (Agilent 81150A) was used to apply the pre- and collection bias which were amplified by a home-built amplifier. The currents flowing through the devices were measured via a 50 Ω resistor and recorded with an oscilloscope (Yokogawa DL9140). The pulse generator was triggered with a fast photodiode (EOT, ET-2030TTL). By applying the shortest possible delay between excitation and extraction of 4–6 ns the generation of free charge carriers could be measured.

XRD: The XRD measurements were performed using a PANalytical X'Pert Pro MRD materials research diffractometer equipped with a Cu tube, X-ray lens and Eulerian cradle. Prior to the measurements, each sample has been aligned in z-direction (sample height) and omega (sample tilt). Out-of-plane and in-plane XRD patterns were recorded in Theta-2 Theta geometry in the 2 Theta range from 4° to 50°. For the out-of-plane measurements a step size of 0.04° and an integration time of three seconds was selected. Since the diffraction volume was much less for in-plane measurements the integration time was increased to 10 seconds. The pole figures of the peaks under investigation were recorded at their corresponding 2 Theta positions covering a full phi rotation (0°-360°) and a psi angle ranging from 0° to 85°. An integration time of one second and a step size of 5° in phi and psi space, respectively, was chosen.
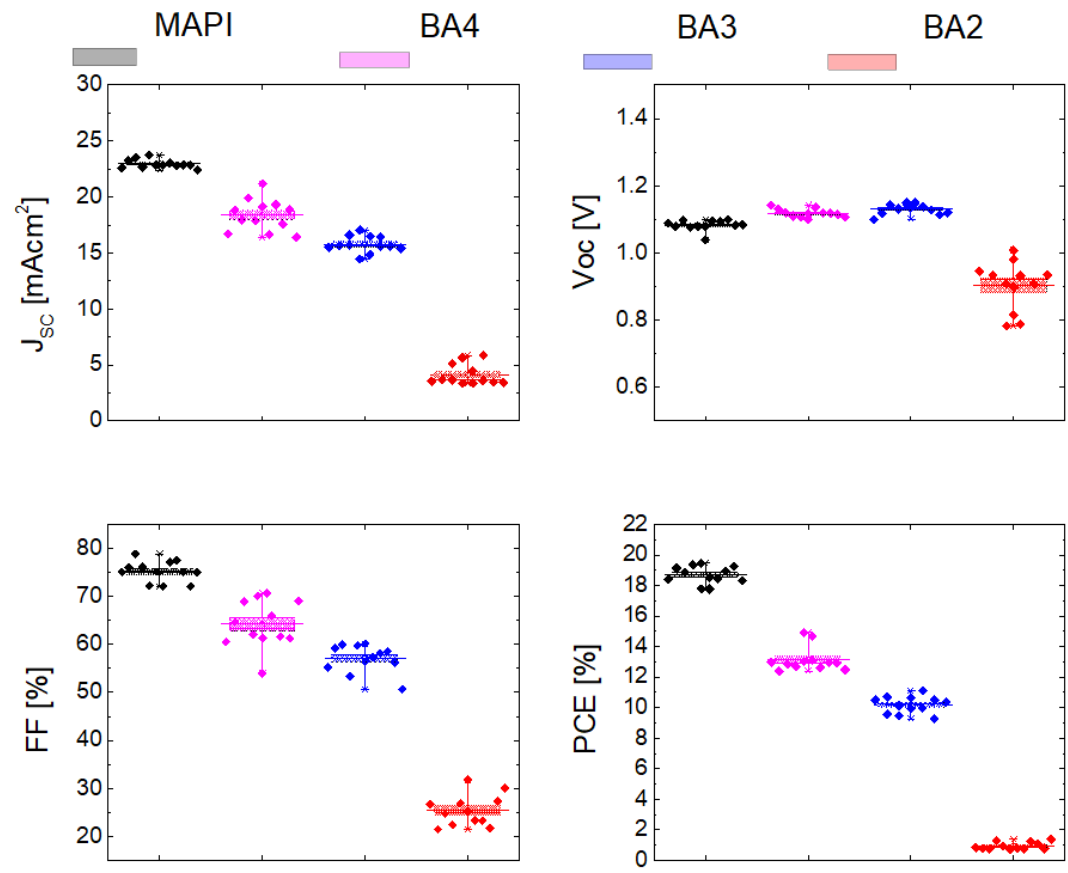
Supplementary Figure S1. *Device statistics of 6 mm^2-sized perovskite solar cells (in a p-i-n configuration ITO/PTAA/PFN-Br/perovskite/C60/BCP/Cu) showing the change in the solar cell parameters by changing the number of the [PbI$_6$]$^{4-}$ layer sheets.*
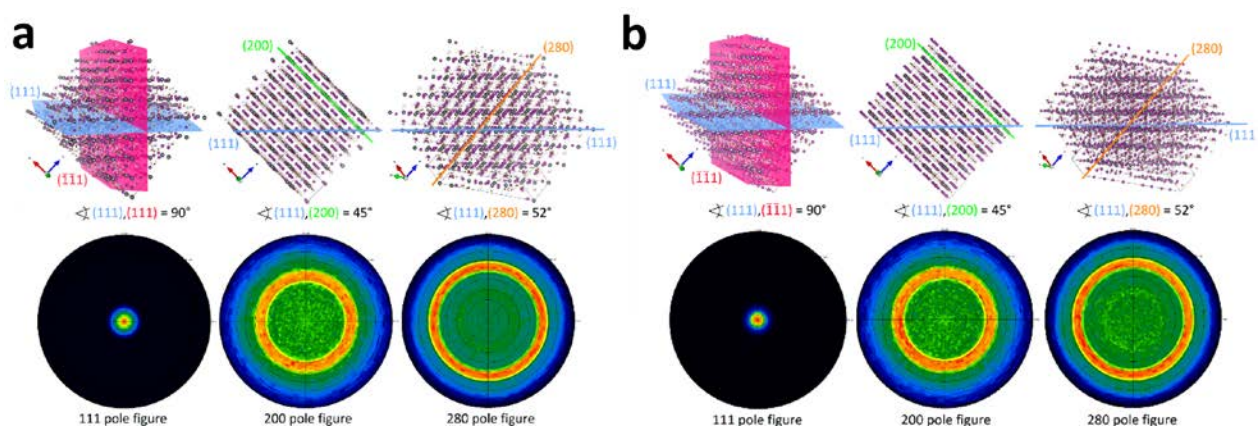
Supplementary Figure S2. *Schematics of the (a) n = 3 and (b) n = 4 RPP structures showing the orientation of the (200) and (280) lattice planes with respect to the (111) lattice plane. The intensity maxima visible in the pole figures appear at positions expected for a two-dimensional material with orthorhombic symmetry.*

The pole figures were recorded to support the findings made with the out-of-plane and in-plane XRD. Provided the perovskite thin films are grown in a layered structure with a very confined growth direction leading to a strong preferred orientation, the pole figures should show features exhibited both by single-crystal and polycrystalline thin films. Regarding the single-crystalline behavior, the position(s) and the number of intensity maxima in the pole figure are determined by symmetry. On the other hand, the polycrystalline nature is reflected by the numerous crystallites that are statistically oriented around the [111] axis (i.e., the fiber axis), thus, smearing out the intensity maxima to concentric rings. The 111 pole figure shows an intensity maximum at psi around 0° (psi refers to the tilt angle of the sample in the X-ray diffractometer), which corresponds to the out-of-plane measurement (i.e., the measured lattice planes are parallel to the substrate). Another intensity maximum would appear at psi = 90°, though, the pole figure measurements cannot be performed at such high psi angles. However, this orientation can be accessed by the in-plane measurements.
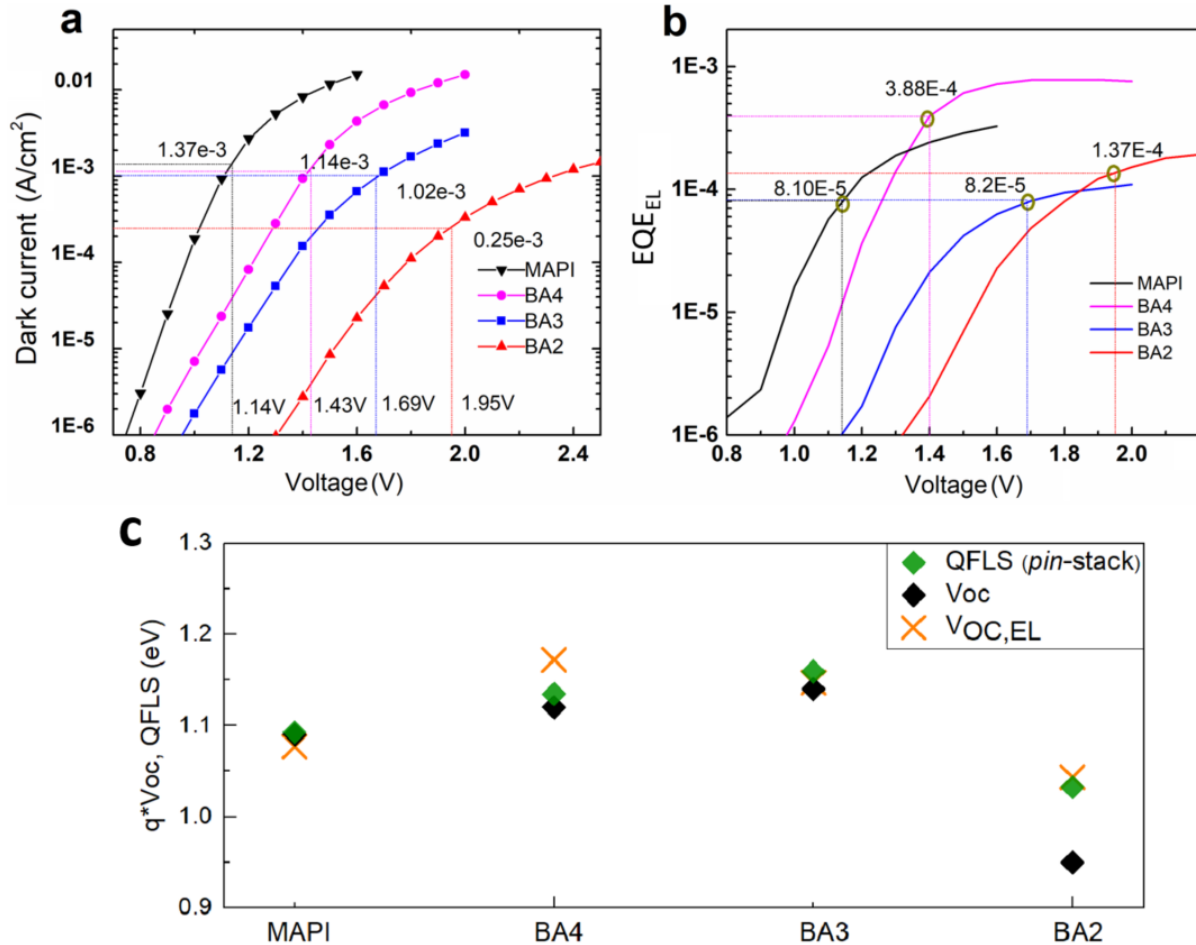

Supplementary Figure S3. *The EQE_{EL} of the BA and MAPI devices. (a) Dark current versus applied voltage. The bias at which the dark injection current equals the generation current density is marked. (b) The EQE_{EL} as a function of applied forward bias of the perovskite devices. The EQE_{EL} is obtained under conditions where dark injection current equals the generation current density. (c) Under these conditions the*

predicted V_{OC} (using the EQE_{EL} instead of the PLQY in equation 1) matches closely the quasi-Fermi level splitting of the p-i-n-stacks).
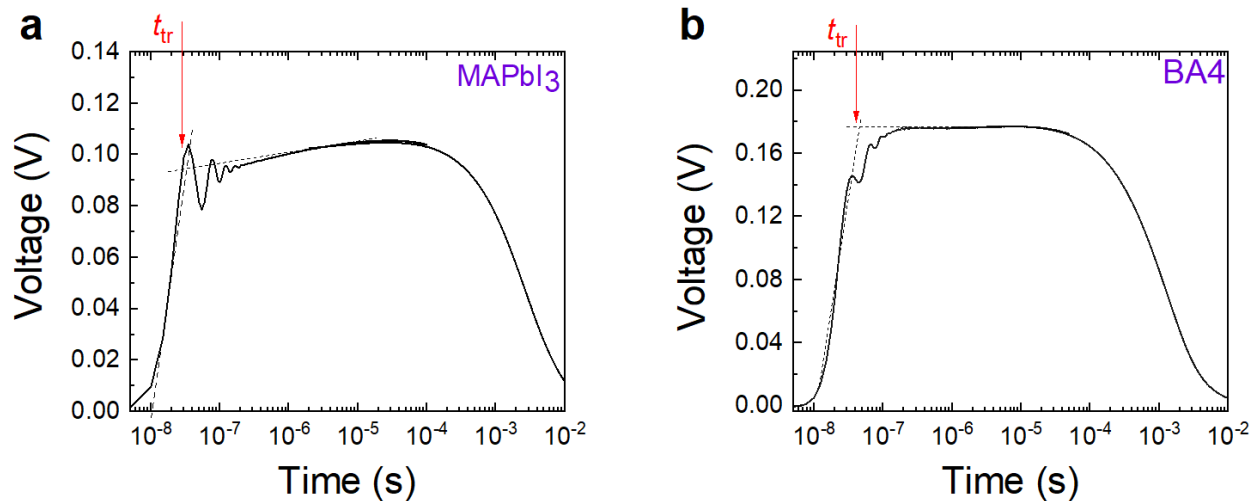
Supplementary Figure S4. *Integral time of flight transients measured on (a) MAPI and (b) BA4 at a load resistance of 1 MΩ after a ns laser excitation. The horizontal red line marks the transit time (t_{tr}) of charges through the device. We note, in the case of MAPI, a small amount of charge (<10%) is extracted at longer times >t_{tr}, which could be related to de-trapping of carriers or the displacement of ions due to the continuous periodicity in this system, which may allow ions to travel on these time scales.*
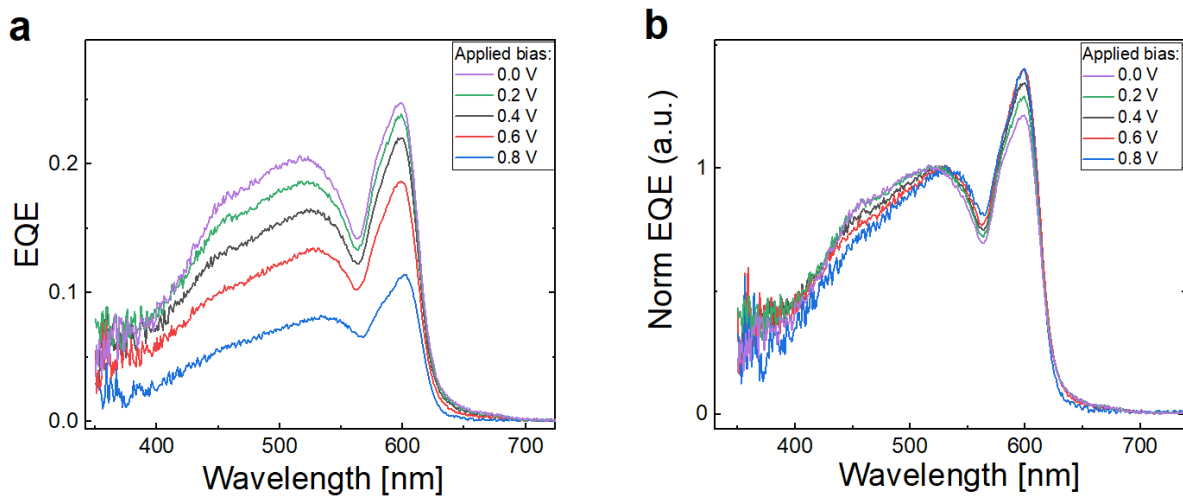
Supplementary Figure S5. *(a) The bias dependent EQE spectrum of the BA2 system displays a distinct feature at 600 nm (which is assigned to the absorption of excitons). However, the feature does not depend on the applied forward bias which is consistent with field-independent exciton dissociation. This is shown in panel (b) where the EQE spectrum was normalized to the EQE at 530 nm.*